

The Effects of Tilt on the Images of Black Hole Accretion Flows

Christopher J. White¹, Jason Dexter², Omer Blaes³, and Eliot Quataert⁴ ¹ Kavli Institute for Theoretical Physics, University of California Santa Barbara, Kohn Hall, Santa Barbara, CA 93107, USA ² JILA and Department of Astrophysical and Planetary Sciences, University of Colorado Boulder, Boulder, CO 80309, USA Department of Physics, University of California Santa Barbara, Broida Hall, Santa Barbara, CA 93106, USA ⁴ Department of Astronomy, University of California Berkeley, 501 Campbell Hall, Berkeley, CA 94720, USA Received 2020 January 7; revised 2020 March 15; accepted 2020 March 27; published 2020 April 30

Abstract

We analyze two 3D general-relativistic magnetohydrodynamic accretion simulations in the context of how they would manifest in Event Horizon Telescope (EHT) observations of supermassive black holes. The two simulations differ only in whether the initial angular momentum of the plasma is aligned with the rapid (a = 0.9) spin of the black hole. Both have low net magnetic flux. Ray tracing is employed to generate resolved images of the synchrotron emission. When using parameters appropriate for Sgr A* and assuming a viewing angle aligned with the black hole spin, we find the most prominent difference is that the central shadow in the image is noticeably eccentric in tilted models, with the ring of emission relatively unchanged. Applying this procedure to M87 with a viewing angle based on the large-scale jet, we find that adding tilt increases the angular size of the ring for fixed black hole mass and distance, while at the same time increasing the number of bright spots in the image. Our findings illustrate observable features that can distinguish tilted from aligned flows. They also show that tilted models can be viable for M87, and that not accounting for tilt can bias inferences of physical parameters. Future modeling of horizon-scale observations should account for potential angular momentum misalignment, which is likely generic at the low accretion rates appropriate for EHT targets.

Unified Astronomy Thesaurus concepts: Accretion (14); Magnetohydrodynamics (1964); Magnetohydrodynamical simulations (1966); Relativistic disks (1388); Relativistic fluid dynamics (1389); General relativity (641); Supermassive black holes (1663); Low-luminosity active galactic nuclei (2033)

1. Introduction

The Event Horizon Telescope (EHT) can now produce resolved images of black hole accretion flows. There is a robust observation of a ring of light around the supermassive black hole in M87 (The Event Horizon Telescope Collaboration 2019a, EHT I), with observations of polarization, as well as of Sgr A*, coming soon. Additionally, we expect the near future to feature even more detailed observations of this sort, with additional interferometric baselines, more sensitivity, and alternate frequencies (The Event Horizon Telescope Collaboration 2019b, EHT II).

These observational capabilities allow unprecedented direct comparison to general relativistic (GR) simulations of black hole accretion flows. From the perspective of magnetohydrodynamics (MHD), such flows are generally characterized by the black hole mass and spin, the density scale of the accreting matter, the geometrical thickness of the flow, and the strength and configuration of the magnetic field. The flow is expected to be geometrically thick for both M87 and Sgr A* (Narayan et al. 1998; Blandford & Begelman 1999; Yuan & Narayan 2014), and the effects of varying spin, disk magnetization, and to a limited extent electron temperature prescription are considered in a library of simulation images in The Event Horizon Telescope Collaboration (2019c, 2019d, hereafter EHT V, EHT VI).

However, there exists another important parameter that can have a significant impact on the appearance of an accretion flow: the misalignment between the black hole spin and the angular momentum of the infalling matter. In the case of lowluminosity active galactic nuclei (AGNs) such as M87 and Sgr A*, we do not expect this matter to be aligned with the spin at large radii. The gas angular momentum cannot be quickly torqued into alignment with the black hole spin given the geometrically thick disks present at low accretion rates (\dot{M}) , nor can a black hole of mass M be torqued into alignment with the disk via accretion of angular momentum except on timescales comparable to M/\dot{M} . Early GR simulations of such flows were performed by Fragile & Anninos (2005) and Fragile et al. (2007), who reported a number of qualitative differences between aligned and tilted flows. The disks become warped and twisted by differential Lense-Thirring precession, and a pair of standing shocks can develop (Fragile & Blaes 2008; Generozov et al. 2014).

These standing shocks in particular may dissipate a large amount of kinetic energy locally, heating electrons and causing nonaxisymmetric emission. From the parameter survey of White et al. (2019), we expect this dissipation in standing shocks to be comparable to the dissipation arising from turbulence and magnetic reconnection throughout the rest of the accretion disk whenever the dimensionless spin is sufficiently large, $a \gtrsim 0.9$, and the flow is sufficiently tilted, with an inclination $i \gtrsim 8^{\circ}$. Indeed, $i = 15^{\circ}$ models of Sgr A* have been shown to differ from aligned models in 230 GHz images (Dexter & Fragile 2013).

Here we investigate these effects further, contrasting the appearances of two GRMHD models, one aligned and one tilted, in different contexts. Section 2 describes the simulations and the subsequent ray tracing used to produce images comparable to what is seen by the EHT. In Section 3 we illustrate the effects of tilt in three different settings. First, we consider images as seen when looking along the spin axis, where the effects of the standing shocks are most intuitive, modeling Sgr A* (whose orientation is currently not well constrained). We then consider the same system but viewed 45°

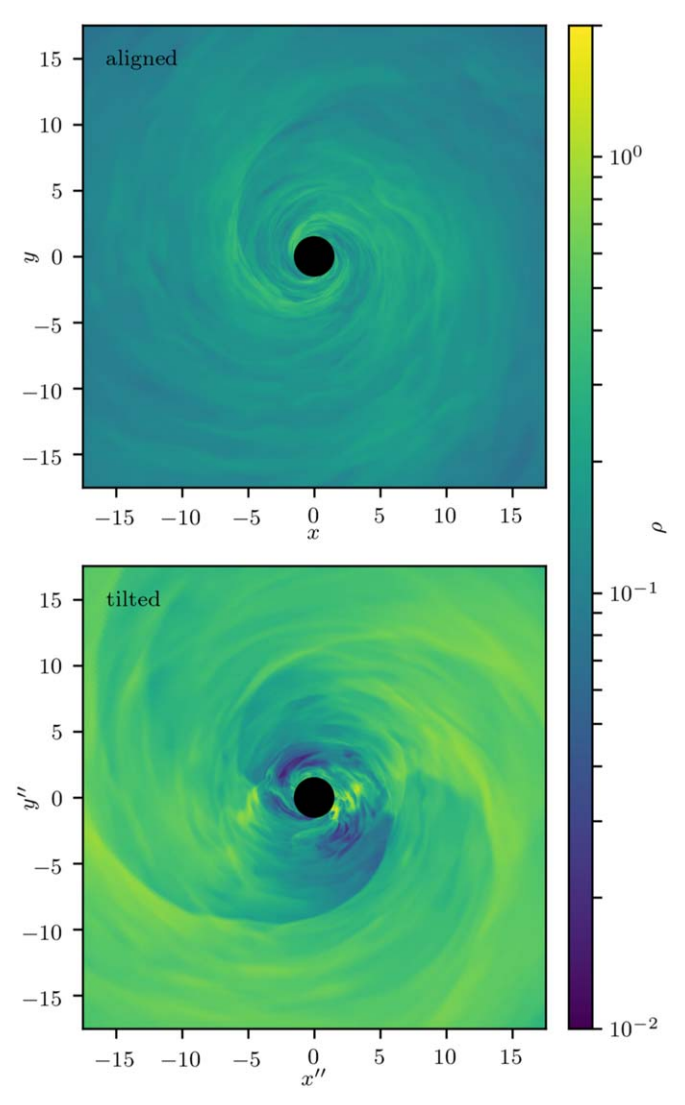


Figure 1. Midplane slices of density at the end of the two simulations. In the tilted case, the midplane is warped and twisted to follow the shell-averaged angular momentum of the disk. There are stronger density contrasts in the tilted case than in the aligned case.

off the spin axis. Finally, we analyze the case of M87, where the orientation can be inferred from observations at large scales. Here tilted disk models produce asymmetric ring (crescent) morphologies that appear compatible with the EHT image.

We will often refer to "rings" and "shadows," by which we simply mean the structures in images at current EHT resolution. These general terms will not necessarily refer to the photon ring or black hole shadow, which are fixed properties of the spacetime and do not depend on the structure of the surrounding emission as long as it extends inside of the black hole photon orbit. Our goal is to provide a sense of what observable properties would signify the presence or absence of angular momentum misalignment. Our results on shadow shape and size have implications for GR tests based on the properties of EHT images, unless the direct accretion flow emission can be separated from that corresponding to the photon ring itself, as we discuss in Section 4.

Throughout this work, quantities with units omitted are taken to be in geometric units appropriate for GRMHD simulations around a black hole of mass M: length in units of GM/c^2 , time in units of GM/c^3 , and density scaled arbitrarily.

2. Numerical Procedure

2.1. GRMHD Simulations

We use the GRMHD code <code>Athena++</code> (White et al. 2016) to evolve two similar accretion flows around a black hole with spin a=0.9, one aligned with the black hole spin and the other tilted. In both cases we use spherical Kerr–Schild coordinates $(t,\,r,\,\theta,\,\phi)$ with a statically refined grid. The root grid has 56 cells geometrically spaced in radius from $r\approx0.926~r_{\rm hor}$ (the horizon is at $r_{\rm hor}\approx1.44$) to r=100, 32 cells uniformly spaced in θ from pole to pole, and 44 cells uniformly spaced in ϕ from 0 to 2π . Three nested levels of mesh refinement are added, each doubling resolution in three dimensions. The highest effective resolution of 448 \times 256 \times 352 (239 cells per decade in radius) is achieved everywhere within 50°.625 of the midplane.

The aligned simulation is initialized with a hydrostatic torus according to the prescription of Fishbone & Moncrief (1976), with inner edge r=15, pressure maximum at r=25, adiabatic index $\Gamma=4/3$, and peak density $\rho=1$. A poloidal magnetic field is added using the vector potential

$$A_{\phi} \propto (\max(p_{\text{gas}} - 10^{-8}, 0)^{1/2} r^2 \sin \theta$$

 $\times \sin(\pi L(r; 16, 34)) \sin(\pi L(\theta; 70^{\circ}, 110^{\circ})),$ (1)

with A_r , $A_\theta = 0$. Here $L(x; x_{\min}, x_{\max})$ is the linear ramp function that runs from 0 for $x \le x_{\min}$ to 1 for $x \ge x_{\max}$.

The tilted simulation applies the Fishbone & Moncrief solution to the coordinates (t, r, θ', ϕ') , with

$$\theta' = \cos^{-1}(\cos i \cos \theta + \sin i \sin \theta \cos \phi), \tag{2a}$$

$$\phi' = \tan^{-1}(\sin\theta\sin\phi, -\sin i\cos\theta + \cos i\sin\theta\cos\phi)$$
 (2b)

being the standard angles obtained by tilting spherical coordinates by an inclination $i=24^{\circ}$ toward $\phi=0^{\circ}$. The torus is no longer in exact equilibrium, though the addition of a magnetic field causes this in any event. Here we apply the vector potential

$$A_{\phi'} \propto \max(\rho - 0.2, 0), \tag{3}$$

with A_r , $A_{\theta'} = 0$.

In both cases we have a magnetic field consisting of a single set of nested loops in the poloidal plane. We normalize the fields such that the density-weighted average of plasma $\beta^{-1} \equiv p_{\rm mag}/p_{\rm gas}$ is 0.01.

Both simulations are run to a time of t = 10,000. As expected, the structures of the flows differ in the two cases. Figure 1 shows midplane slices of density at the end of the simulation. In the tilted case, the surface used for the slicing, denoted with two primes, is warped and twisted in order to be orthogonal to the gas angular momentum at each radius. The angle between the surface normal and the black hole spin direction can exceed the initial inclination, reaching 44° at small radii. Using the same density scale, one can see much stronger density contrasts in the tilted case. These result from the standing shocks created in misaligned disks, as explained by Fragile & Blaes (2008).

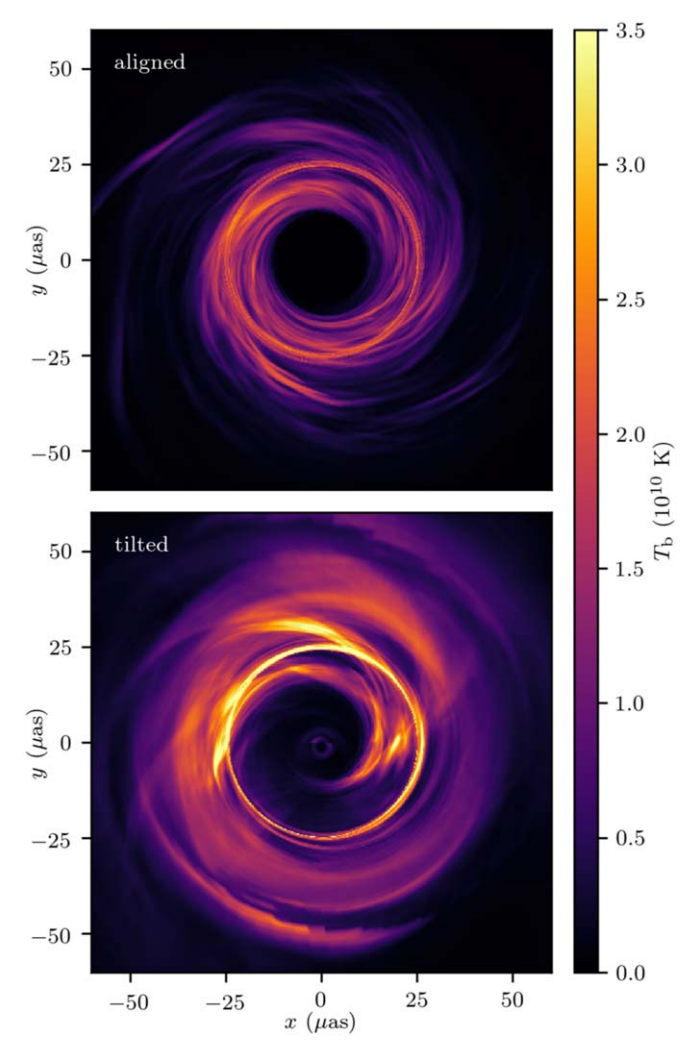


Figure 2. Images created from a snapshot from each simulation, modeled on Sgr A^* assuming a nearly face-on viewing angle. The accretion flow is clockwise in both images, with the southern spin axis pointing toward the camera 3° off the line of sight (pointing down when projected onto the image plane). The tilted disk induces the foreground nonaxisymmetric shock seen in emission, spiraling clockwise inward just to the right of the center of the image.

2.2. Ray Tracing

We use the GR ray tracing code grtrans (Dexter & Agol 2009; Dexter 2016) to process snapshots from the simulations into images. The camera is located at coordinates (r_0, θ_0, ϕ_0) . We set $r_0 = 50$; in all cases there is negligible emission and absorption beyond this radius. A grid of 512^2 pixels is created in the image plane, with a field of view of $24 \ GM/c^2$ on each side. Each ray traced back from the image plane through the simulation is sampled at 1600 points.

Here we only consider total intensity (Stokes I) images (only tracking polarization internally during ray tracing) at 230 GHz as produced by the emission and absorption of thermal synchrotron radiation along each ray. The scale-free MHD snapshots are given physical units by setting the black hole mass M and fluid density scale $[\rho]$. The latter is adjusted in order to match observed 230 GHz flux density, fixing the time-averaged mass accretion rate onto the black hole in the process. In all cases the fluid temperature in the simulation is converted to electron temperature according to the same ansatz as in

Mościbrodzka et al. (2016), assuming an ion-to-electron temperature ratio of

$$\frac{T_{\rm i}}{T_{\rm e}} = \frac{R_{\rm low} + R_{\rm high}\beta^2}{1 + \beta^2},\tag{4}$$

with $R_{\rm low}=1$ and $R_{\rm high}=10$. This is the same prescription used in EHT V, where $R_{\rm low}$ is also kept at 1 and $R_{\rm high}$ is varied over a range of plausible values from 1 to 160. We choose to use a single intermediate $R_{\rm high}$ in order to focus on the effects of accretion flow geometry. While changing this parameter can redistribute intensity within the image, possibly changing the overall size of the observed ring, we do not expect variations in $R_{\rm high}$ to qualitatively change aspects of image morphology that arise due to flow geometry. We note that models developed to capture the effects of turbulent heating may not be appropriate for shock-heated regions in the tilted flows, and that better prescriptions may need to be developed for these cases.

When applying the simulations to a face-on model of Sgr A*, we choose $M = 4.152 \times 10^6 M_{\odot}$ and place the source at a distance D = 8.178 kpc, following the inferred values in The GRAVITY Collaboration (2019). We seek to have the average flux from our snapshots match $F_{\nu} = 2.4 \text{ Jy}$ (Doeleman et al. 2008), which results in choosing [ρ] = 1.7 \times 10⁻¹⁶ g cm⁻³ in the aligned case and $[\rho] = 4.8 \times 10^{-17} \text{ g cm}^{-3}$ in the tilted case. With these scales we can convert the accretion rates in the simulations, averaged from t = 8000 to t = 10,000, to the physical values of $\dot{M} = 8.4 \times 10^{-9} M_{\odot} \text{ yr}^{-1}$ in the aligned case and $\dot{M} = 5.1 \times 10^{-9} M_{\odot} \text{ yr}^{-1}$ in the tilted case. Defining an Eddington accretion rate of $\dot{M}_{\rm Edd} = 10 \cdot 4\pi GMm_{\rm p}/c\sigma_{\rm T}$, these correspond to 9.1 imes 10^{-8} \dot{M}_{Edd} and 5.5 imes 10^{-8} \dot{M}_{Edd} . Here we fix the viewing angle $\theta_0 = 177^{\circ}$ and we choose $\phi_0 = 0^{\circ}$, though the symmetry of the system means the latter has little effect. The images are rotated such that the south pole (the one pointed toward the camera) has a small projection in the plane of the image at a position angle of 180° (toward the bottom), with the flow moving clockwise.

For the inclined model of Sgr A*, we keep the same mass, distance, and flux. The viewing angle is $\theta_0=135^\circ$, $\phi_0=0^\circ$. Again the southern (near) pole points to the bottom of the image and the matter is moving clockwise. In this case, the density scale $[\rho]$ is 1.6×10^{-16} g cm⁻³ in the aligned case and 5.6×10^{-17} g cm⁻³ in the tilted case. The accretion rates are 7.7×10^{-9} M_\odot yr⁻¹ (8.4 \times 10⁻⁸ $\dot{M}_{\rm Edd}$) and 6.0×10^{-9} M_\odot yr⁻¹ (6.5 \times 10⁻⁹ $\dot{M}_{\rm Edd}$), respectively.

With M87 we use the inferred mass $M=6.5\times10^9~M_{\odot}$ and combined distance measurement D=16.8 Mpc from EHT VI (the distance is derived from the measurements in Blakeslee et al. 2009; Bird et al. 2010; Cantiello et al. 2018), as well as the flux $F_{\nu}=0.98$ Jy (Doeleman et al. 2012), resulting in $[\rho]$ being 4.8×10^{-18} g cm⁻³ and 6.9×10^{-19} g cm⁻³ in the aligned and tilted cases, respectively. This implies physical accretion rates of $\dot{M}=5.8\times10^{-4}~M_{\odot}~\rm yr^{-1}$ ($4.0\times10^{-6}~\dot{M}_{\rm Edd}$) and $\dot{M}=1.8\times10^{-4}~M_{\odot}~\rm yr^{-1}$ ($1.2\times10^{-6}~\dot{M}_{\rm Edd}$), respectively. In both cases we use a viewing angle $\theta_0=163^\circ$ (agreeing in magnitude with Mertens et al. 2016), fixing $\phi_0=0^\circ$. Here we rotate the image such that an approaching jet aligned with the spin axis will have a position angle of 288° (toward the right and slightly up), in agreement with the large-scale jet seen in M87 (Walker et al. 2018). The accretion flow is clockwise.

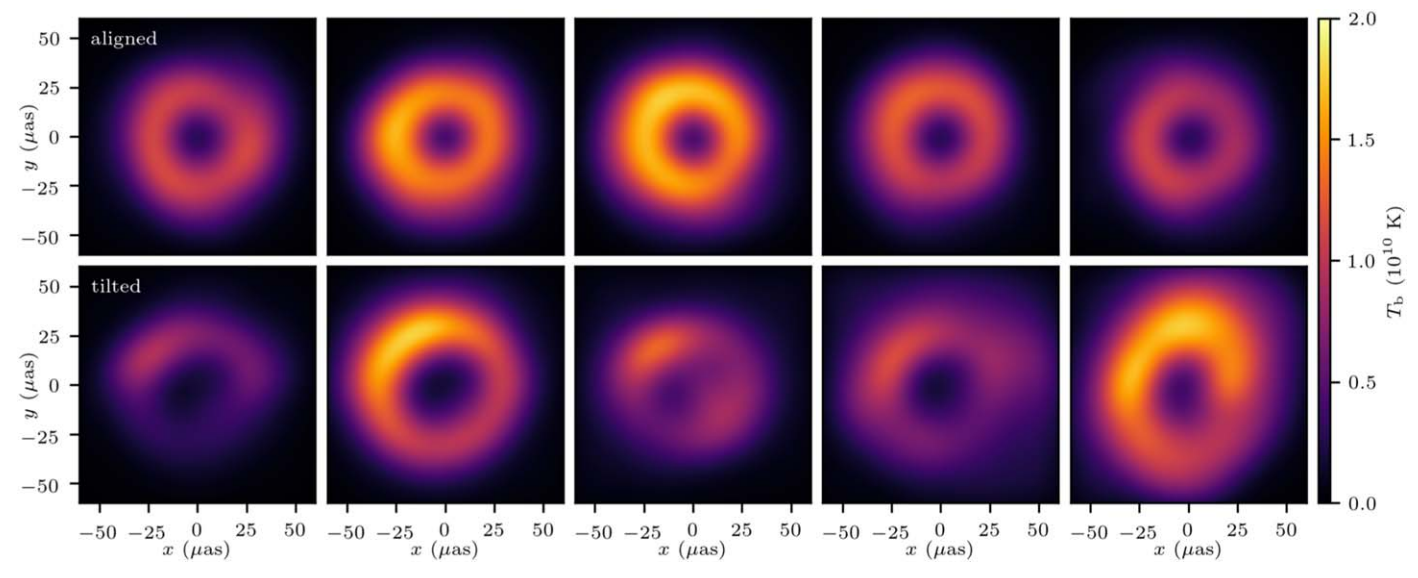


Figure 3. Blurred images modeled on Sgr A* with a nearly face-on viewing angle for the aligned (top) and tilted (bottom) simulations. The camera position and orientation are the same as those in Figure 2. The snapshots span a time range of 11 hr. While the bright shock interior to the nominal shadow in Figure 2 is no longer evident due to blurring, its effect is to make the shadows eccentric in the tilted cases.

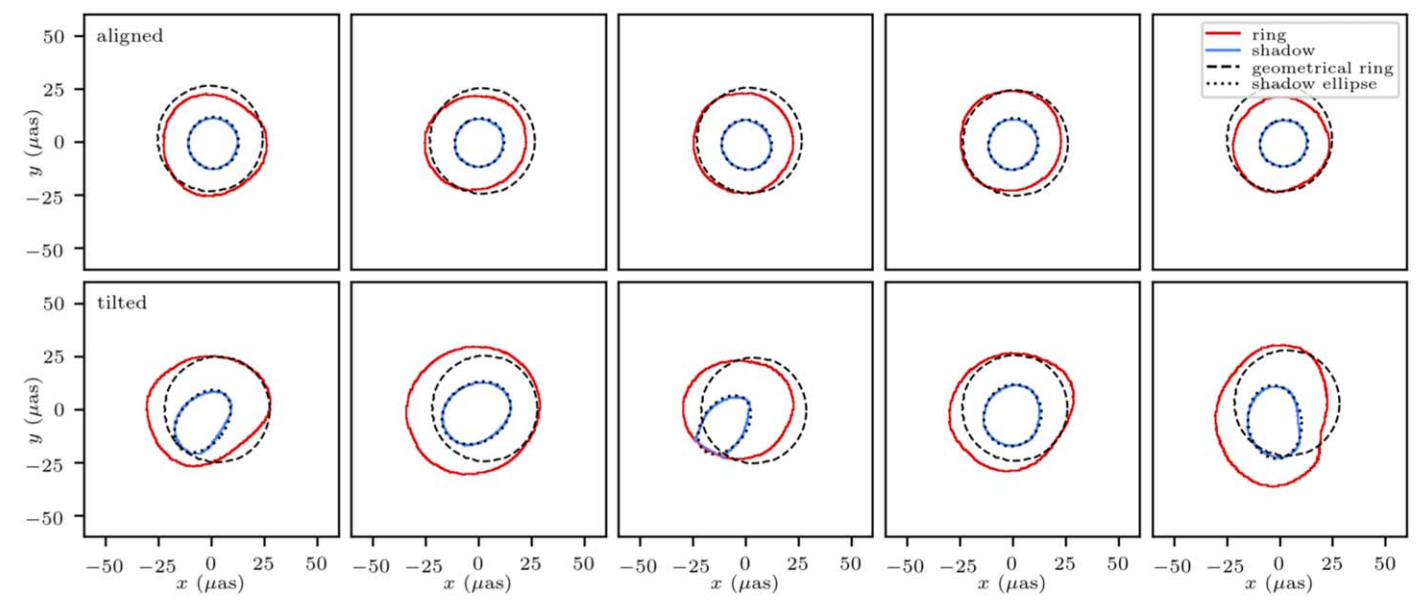


Figure 4. Contours for the ring (red), shadow (blue), geometrical ring (black dashed), and best-fit shadow ellipse (black dotted) for the aligned (top) and tilted (bottom) simulations modeling Sgr A* face-on. The snapshots used are those shown in Figure 3.

In the process of ray tracing, we can delineate the boundary between rays that trace back into the black hole and those that do not. We will refer to this boundary as the "geometrical ring," also known as the photon ring.

In several cases we will consider a set of 21 snapshots uniformly sampled in time from t=8000 to t=10,000. The separation of $\Delta t=100$ between snapshots is larger than the correlation time at the small radii of interest in these turbulent accretion flows, so these samples can be considered independent.

3. Image Analysis

3.1. Face-on Shadow Shape in Sgr A*

First we consider the face-on case. Here we use parameters suitable for Sgr A*, where the inclinations of both the spin axis

and the gas angular momentum to the line of sight are currently poorly constrained. For example, one might expect the system to prefer alignment with the clockwise disk (that is more edge-on than face-on) of stars within 0.3 Mpc (Paumard et al. 2006; Beloborodov et al. 2006), but at the same time orbital motion in a nearly face-on system is consistent with the near-infrared centroid motion found by the GRAVITY instrument (GRAVITY Collaboration 2018). We choose to first model the system with face-on spin, where the connection between shock structure and image features is clearest.

Figure 2 shows images constructed from high-resolution snapshots at the end of the simulation (t = 10,000). Here we can clearly see a breaking of axisymmetry caused by the standing shocks in the tilted disk, as well as by Doppler shifts in the parts of the disk moving toward or away from the camera. Importantly, the standing shock seen here is in the

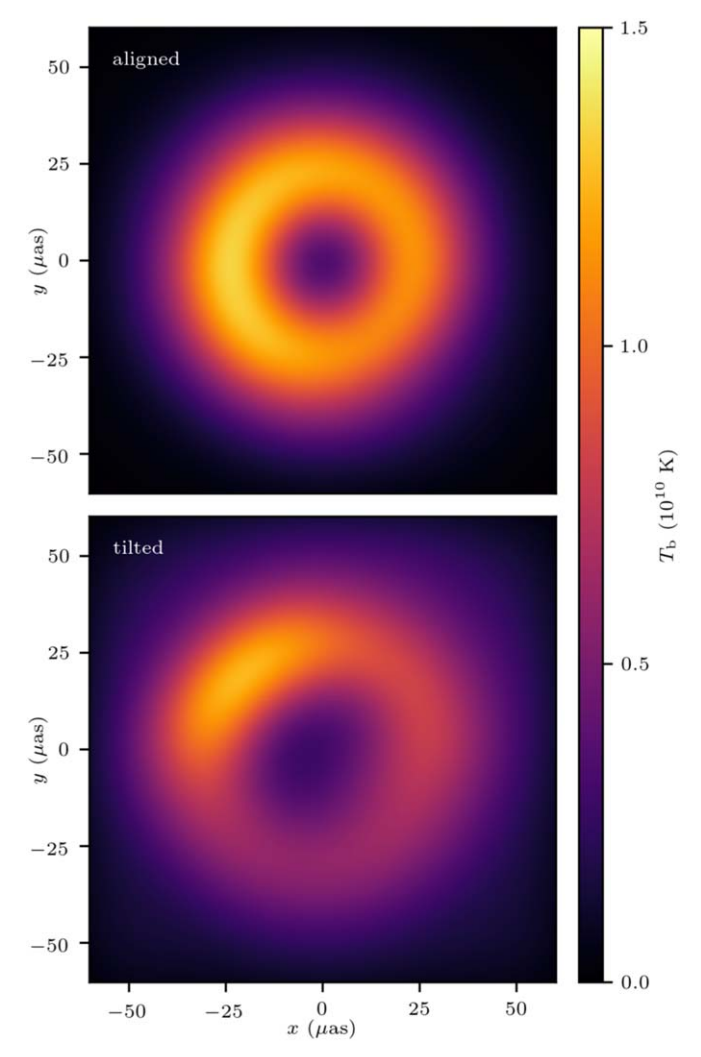


Figure 5. Blurred, time-averaged images modeled on Sgr A* with a nearly face-on viewing angle for the aligned (top) and tilted (bottom) simulations. The camera position and orientation is the same as that for the non-time-averaged images in Figure 3, and the time averaging spans 11 hr. Even with this averaging, the shadow remains distinctly eccentric in the tilted case.

foreground (the disk is geometrically thick with the inner part not entirely optically thin, and the other shock in the background is obscured and distorted), enabling it to be seen at small projected radii where there is only an uninterrupted, circular shadow in the aligned case.

The resolution of Figure 2 is far higher than that of the EHT. We therefore blur the image with a Gaussian kernel with an FWHM of 20 μ as to see if there remain any features capable of distinguishing tilted from aligned flows. This kernel is appropriate for modeling EHT data in the image plane (EHT II). In particular, we expect the bright, nonaxisymmetric feature near the center of the lower panel of Figure 2 to affect the shadow shape even if the ring remains relatively circular.

The top panels in Figure 3 show the results of this blurring process on five snapshots from the aligned simulation, equally spaced in time from t = 8000 to t = 10,000 (a span of approximately 11 hr for Sgr A*). The bottom panels show the corresponding snapshots from the tilted simulation. By eye, adding tilt appears to make the ring brightness slightly less symmetric and to make the shadow less circular.

We use the following procedure to quantify the shapes of the rings and shadows in the blurred images. From the image

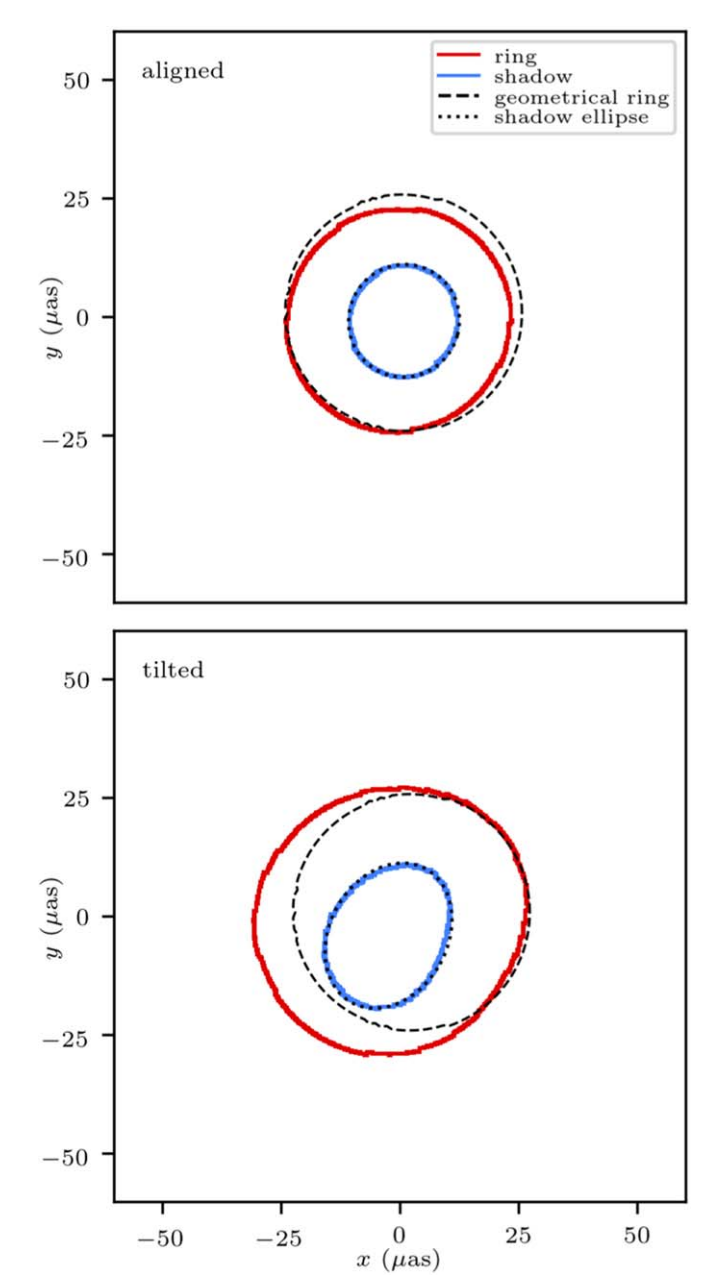


Figure 6. Contours for the ring (red), shadow (blue), geometrical ring (black dashed), and best-fit shadow ellipse (black dotted) for the aligned (top) and tilted (bottom) time-averaged images modeling Sgr A^* viewed face-on. The images used are those shown in Figure 5. As is clear in Figure 5, the time-averaged shadow is noticeably eccentric in the tilted simulation.

center we resample intensity onto 128 radial rays, each with 128 sample points. A ridgeline is found, consisting of each point that is the local maximum of intensity in its ray. A new center is calculated as the centroid of the pixels contained inside this ridgeline, not weighted by intensity, and the ridgeline is recalculated from this new center, ensuring that even a feature offset from the image center is uniformly sampled in angle. This ridgeline is taken to be the ring. We define a ring "roughness" $R_{\rm ring}$ to be the standard deviation of the set of distances from the new center to the ridgeline, divided by the mean of the set. A perfect circle would have a roughness of 0. Our procedure so far is similar to that described in The Event Horizon Telescope Collaboration (2019c, EHT IV), their Section 9.1, for defining the ring.

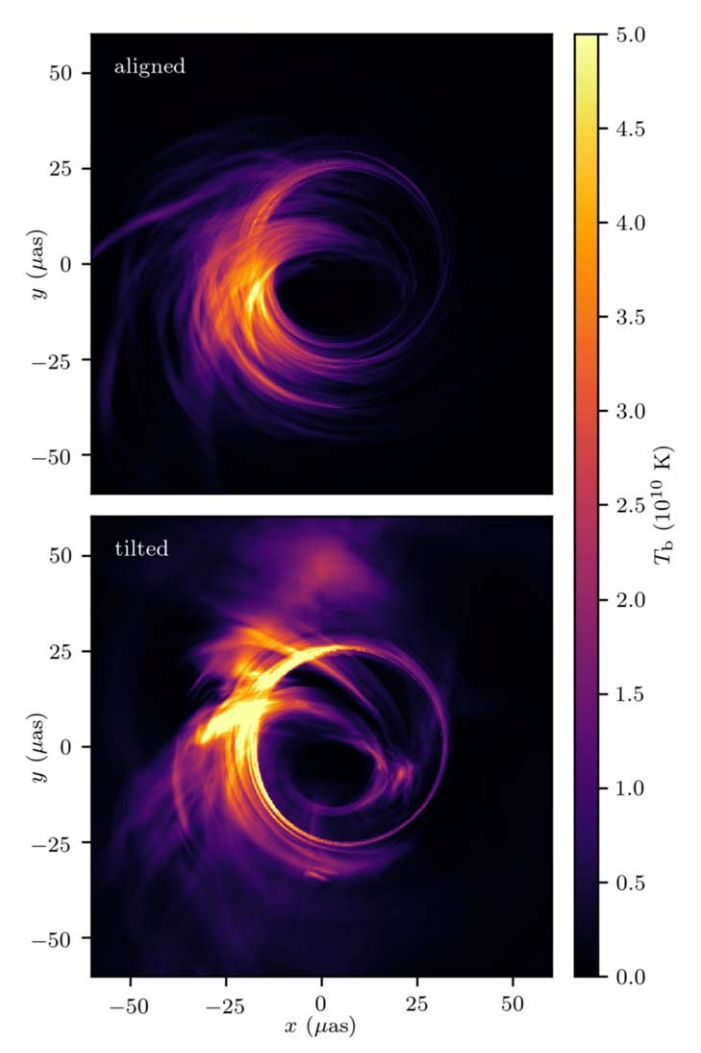


Figure 7. Images created from a snapshot from each simulation, modeled on Sgr A* assuming an inclined viewing angle. The accretion flow is clockwise in both images, with the southern spin axis pointing toward the camera 45° off the line of sight (pointing down when projected onto the image plane). Complex morphology is present in both images.

Next, we define the "shadow" to be the dimmest quartile of pixels inside the ring. Taking the zeroth and first moments of this set of pixels, again not weighted by intensity, yields the size S and center (\bar{x}^1, \bar{x}^2) of the shadow:

$$S = \sum_{\text{shadow}} 1,\tag{5a}$$

$$\bar{x}^i = \frac{1}{S} \sum_{\text{shadow}} x^i. \tag{5b}$$

A shadow contour can be defined by again sampling along rays emanating from this central point, this time finding the radius where the intensity crosses the aforementioned quartile value. This boundary also has an associated roughness value R_{shadow} .

We are particularly interested in the shape of the shadow, so we measure it in another way. Define the second moments

$$M_{ij} = \frac{4}{S} \sum_{\text{shadow}} (x^i - \bar{x}^i)(x^j - \bar{x}^j).$$
 (6)

Arranging the second moments into a matrix, the eigenvalues can be taken to be the squares of the semimajor and semiminor

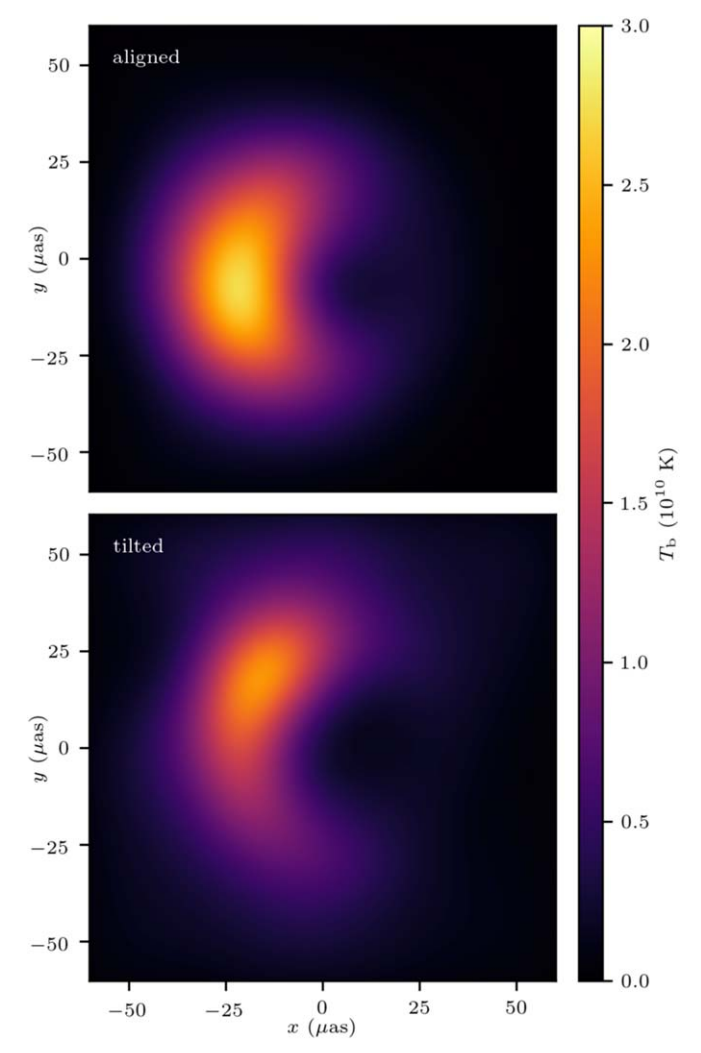


Figure 8. Blurred, time-averaged images modeled on Sgr A* with an inclined viewing angle for the aligned (top) and tilted (bottom) simulations. The camera position and orientation are the same as those for the unblurred snapshots in Figure 7. The time averaging spans 11 hr. Both cases display a crescent, but the image is more asymmetric in the tilted case, and the shadow is significantly eccentric.

axes of an ellipse, with the corresponding eigenvectors indicating the axes' orientations.⁵

Figure 4 shows the contours for the rings and shadows corresponding to the snapshots shown in Figure 3. The contours match what can be seen by eye in the blurred images. We also plot the ellipses obtained from the second moments, and they are generally good fits to the shadow regions.

Using 21 blurred images over the span of time from t = 8000 to t = 10,000 (again, roughly 11 hr for Sgr A*), we calculate the roughness parameter for the ring to be $R_{\rm ring} = 0.027 \pm 0.010$ in the aligned case and $R_{\rm ring} = 0.052 \pm 0.019$ in the tilted case. The reported numbers are the mean plus or minus the standard deviation over the set of snapshots. The tilted rings are slightly more uneven, but only by about one standard deviation.

The shadow roughness parameters for the same set of snapshots are $R_{\rm shadow} = 0.021 \pm 0.011$ and $R_{\rm shadow} = 0.136 \pm 0.055$ for the aligned and tilted cases, respectively. Here there is

⁵ Ellipses are also generated in this way by Shiokawa (2013) in the context of images of tilted disks, but there the focus is on fitting the small region of peak brightness.

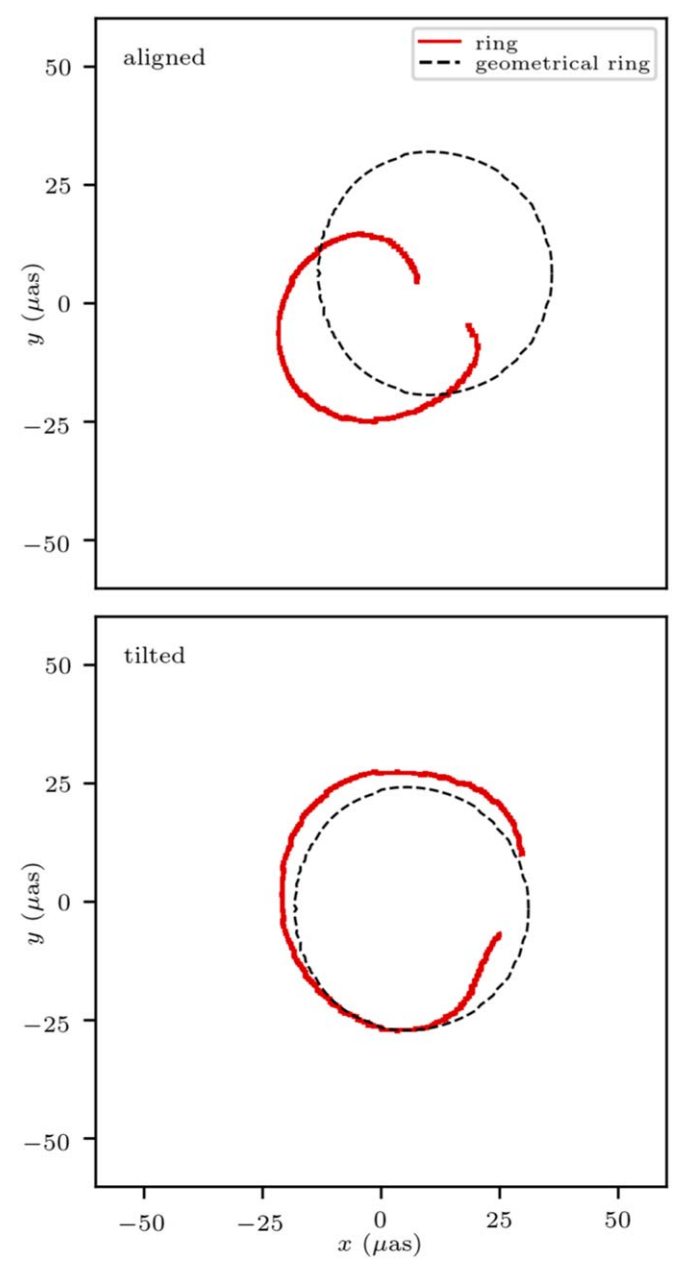


Figure 9. Ring contour (red) and geometrical ring (black dashed) for the aligned (top) and tilted (bottom) time-averaged images modeling Sgr A^* viewed at an angle. The images used are those shown in Figure 8. The ring has a radius approximately 30% larger in the tilted case.

a significant difference: the shadows in the tilted images are distinctly noncircular. The same result is seen when examining the eccentricities of the best-fit ellipses to the shadows, which are measured to be $e_{\rm shadow}=0.291\pm0.085$ for the aligned images and $e_{\rm shadow}=0.69\pm0.11$ for the tilted images. By looking at the shape of the shadow inside the ring, rather than the ring's ridgeline itself, a difference between aligned and tilted accretion flows can be discerned.

The orientations of the major axes of the ellipses fitting the aligned shadows change drastically from one snapshot to the next (a separation of 17 minutes). This is not surprising given the circular nature of these shadows. For the shadows in tilted flows, however, these orientations change slowly in time. The

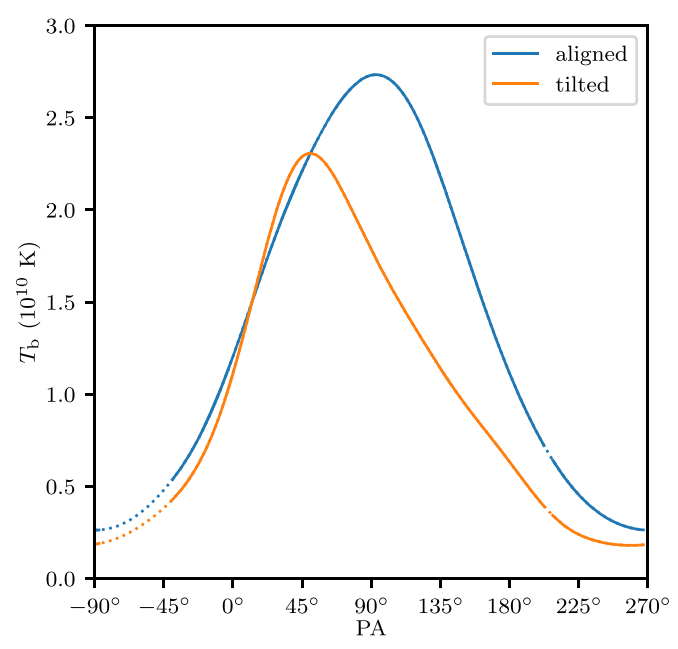


Figure 10. Ridgeline brightness temperatures for the blurred, time-averaged images from the aligned and tilted simulations, modeled to match Sgr A^* as seen at a 45° inclination. The lines are solid where ridgelines are well defined; they are dashed where linear interpolation of radius as a function of position angle is used to locate them. The peak is symmetric in the aligned case and skewed in the tilted case.

average magnitude by which they change from one snapshot to the next is only 13°.

Given the potential rapid variability of Sgr A* relative to the duration of EHT observations $(GM/c^3=20~{\rm s})$, we repeat the above analyses on a time-averaged image. That is, we first apply grtrans to 21 snapshots as before, then average the resulting images in time, then blur the averaged image, and finally measure the ring and shadow properties for the single blurred image. The blurred images are shown in Figure 5, and the corresponding contours are highlighted in Figure 6. The ring roughness is $R_{\rm ring}=0.0147$ in the aligned case and $R_{\rm ring}=0.0304$ in the tilted case. The shadow again shows a greater difference: $R_{\rm shadow}$ is 0.0203 and 0.0998 in the aligned and tilted cases, respectively, and $e_{\rm shadow}$ is 0.209 and 0.641, respectively.

3.2. Sgr A* Viewed from an Angle

Given the present uncertainty in the orientation of Sgr A*, we consider another viewing angle: 45° off the black hole spin axis. Figure 7 shows high-resolution images created from a single snapshot in both the aligned and tilted cases. Unlike in the face-on case, both images are similarly complex and there are no immediately distinguishable features.

As in Section 3.1, we take the blurred, time-averaged image as an appropriate proxy for EHT data. Time averaging the same 21 snapshots spanning t=8000 to t=10,000 (11 hr given the mass $M=4.152\times 10^6~M_\odot$) and applying a 20 μ as Gaussian filter, we obtain the images shown in Figure 8. Images from this inclined viewing angle do not have shadows inside rings that are as well-defined as those in the face-on case when blurred to match the EHT resolution. Still, the shadow can be seen to be significantly eccentric in the tilted image, as with the face-on viewing angle discussed in Section 3.1. The images display a distinct crescent morphology. Importantly, the crescent is

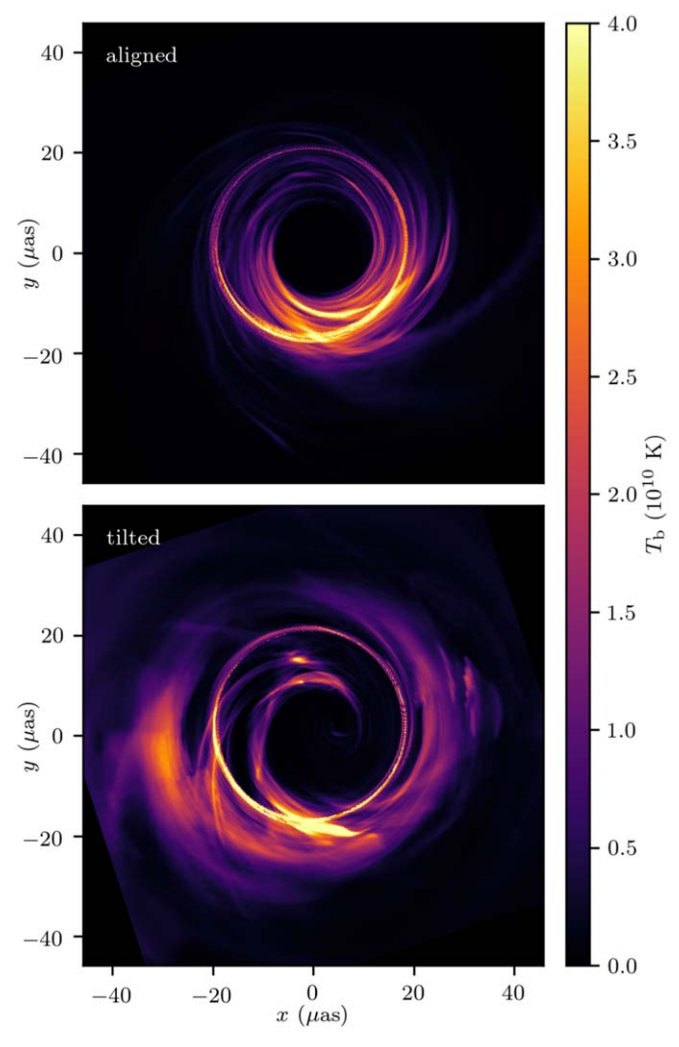


Figure 11. Images from aligned and tilted simulations modeled on M87. The accretion flow is clockwise in both images, with the southern spin axis pointing toward the camera 17° off the line of sight (pointing to the right and slightly up, at a position angle of 288° , when projected onto the image plane). Neither case is axisymmetric, but only the tilted case has the distinct spiral shock detached from the rest of the emission near the center of the image.

symmetric in the aligned case, whereas in the tilted case the southern tail extends farther from the brightness peak.

Using the blurred images, we can define a ridgeline as before, though in some directions the algorithm will fail to find a well-defined intensity maximum. We can still define parts of a ring, as shown in Figure 9. From these plots, it is apparent that the tilted image has a larger ridgeline. The mean distance from the ring center to the ridgeline is $r_{\rm ring} = 19.8~\mu{\rm as}$ in the aligned case and $r_{\rm ring} = 26.2~\mu{\rm as}$ in the tilted case.

In order to sample intensity along the ridgeline, we extend the procedure: whenever a sample location is needed but no ridgeline can be found, the distance of the ridgeline from the central point is linearly interpolated in angle from the nearest angles in either direction for which a local maximum exists. We can then measure intensity along a closed arc. The results, plotted as a function of position angle, are shown in Figure 10. Again, the skewness in the ridgeline intensity in the tilted case is apparent.

3.3. Ring Size and Structure in M87

The same two simulations can be used to model emission from M87, changing the black hole mass, distance, and average flux parameters when ray tracing. Here we do not have as much freedom to choose the viewing angle inclination θ_0 , given the observed large-scale jet oriented 17° off our line of sight. That is, we assume the large-scale jet is aligned with the black hole spin axis, though there are some simulations that suggest this is not the case (Liska et al. 2018). Our choice produces images both aligned and tilted—broadly consistent with M87 observations, with more emission coming from the southern part of the image. Moreover, changing the viewing angle to align the disk normal with the observed jet would not qualitatively change the fact that tilted flows differ from aligned ones by containing intrinsically nonaxisymmetric structure. For example, a highresolution image from each simulation is shown in Figure 11, where even the aligned case now has nonaxisymmetric structure. Still, the tilted case displays a qualitative difference by having a prominent spiral shock penetrate the shadow.

Figure 12 shows five blurred images taken from each simulation, equally spaced over a time span of $8000 \le t \le 10,000$ (a 2.0 yr range for M87's mass). As with the inclined viewing angle for Sgr A*, we often find the intensity ridgeline does not completely enclose the shadow; that is, moving outward from the shadow center the intensity sometimes monotonically decreases. Thus the simple procedure we employed for face-on Sgr A* images fails to define a shadow here. We note this may be an artifact of our simple smoothing prescription; there is a ridgeline in the unblurred image, and a smaller smoothing kernel keeps it intact.

Figure 13 shows the ridgelines corresponding to the blurred snapshots of Figure 12. The lines break where there is no local maximum in the given direction. Using just the parts of the ridgeline that do not require interpolation, the calculated roughness parameter is $R_{\rm ring} = 0.048 \pm 0.012$ in the aligned images and $R_{\rm ring} = 0.083 \pm 0.048$ in the tilted images. The reported numbers are the mean plus or minus the standard deviation over 21 snapshots.

Even though the ring and shadow are somewhat less well defined than for the face-on viewing angle, there are two immediately apparent differences between the sets of aligned images and tilted images. First, the latter has ridgelines that are located farther from the ring center in all directions. As in Section 3.2, we quantify this by measuring a mean distance from ring center to ridgeline, averaging over all rays originating from the ring center. We then take the mean and standard deviation over the set of snapshots. In the aligned case, the average ridgeline radius is $r_{\rm ring} = 12.47 \pm 0.75~\mu{\rm as}$; in the tilted case, it is $r_{\rm ring} = 22.0 \pm 3.4~\mu{\rm as}$.

The other difference is in the regularity of the blurred aligned images relative to the tilted ones. The latter often have multiple distinct bright locations around the ring. To illustrate this better, we walk along the ridgelines and note the brightness temperature as a function of position angle. Figure 14 shows the resulting ring intensities for 21 snapshots in both cases, with dotted lines denoting where interpolation is used to define a sampling location. All aligned ridgelines have a single peak, reflecting the fact that each image consists of a well-defined crescent. On the other hand, most tilted ridgelines have two or three local maxima, reflecting the clumpy nature of the images.

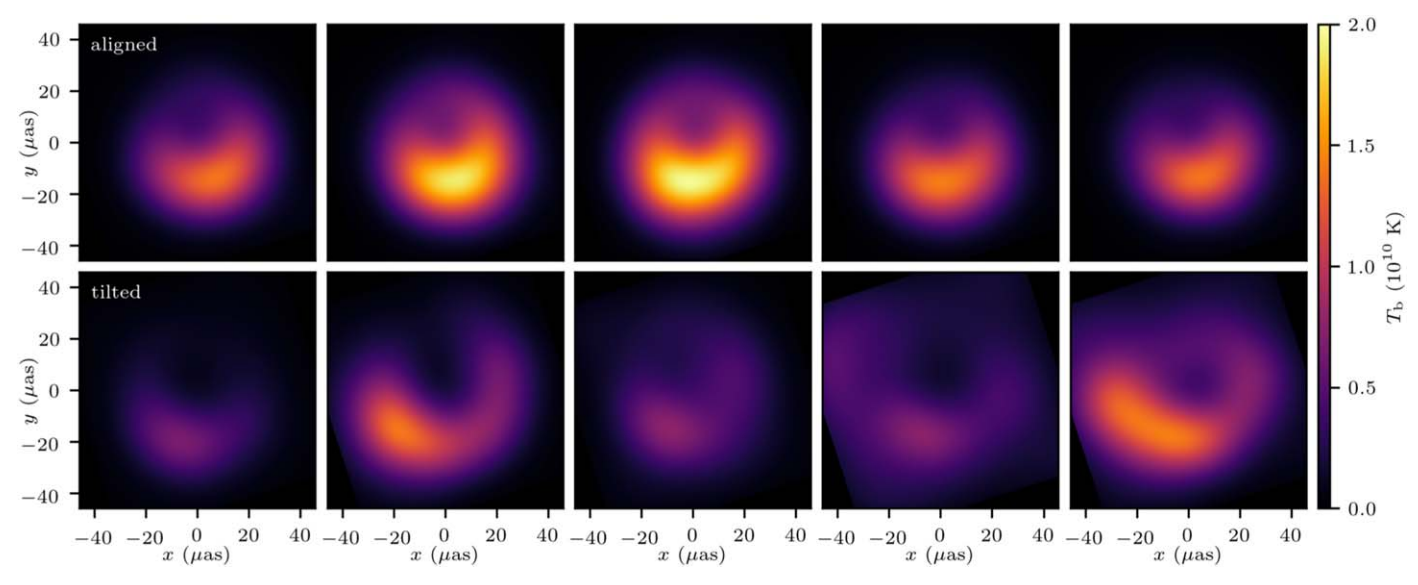


Figure 12. Blurred images modeled on M87 as seen from Earth for the aligned (top) and tilted (bottom) simulations at five different times (separated by a total of 2.0 yr). The camera position and orientation are the same as those in Figure 11. Compared to the face-on images of Sgr A^* in Figure 3, the shadows here are less well defined.

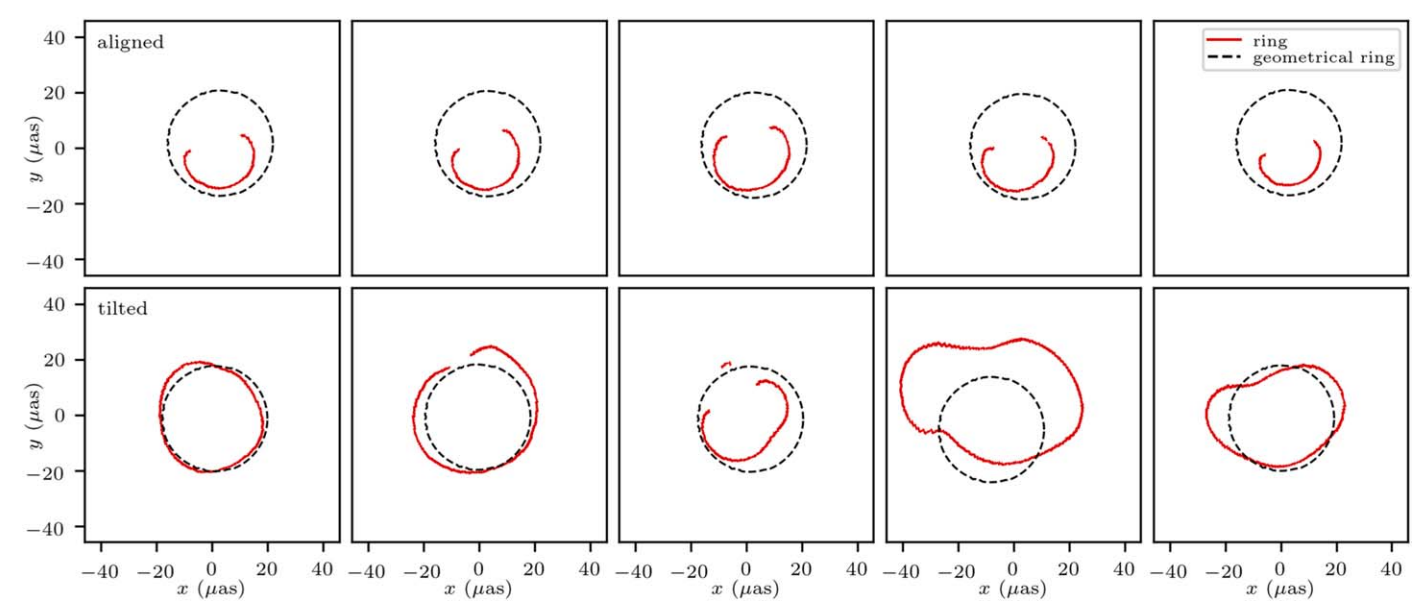


Figure 13. Ring contours (red) and geometrical rings (black dashed) for the aligned (top) and tilted (bottom) simulations modeled on M87. The snapshots used are those shown in Figure 12. The line breaks wherever there is no local maximum and the notion of a ring becomes ambiguous.

4. Implications and Discussion

Misalignment of infalling matter's angular momentum with that of a rapidly spinning black hole can have a significant impact on the dynamics of the accretion flow. A priori we expect such tilt to be common in low-luminosity AGNs and thus to have observable consequences in resolved images as produced by the EHT. We have explored and begun to quantify some of these consequences in SANE (standard and normal evolution, as opposed to magnetically arrested) models of Sgr A* and M87, enabling observations of these systems to provide evidence either for or against the presence of tilt.

A summary of parameters measured from our models is given in Table 1. For completeness, we include values for $r_{\rm ring}$, $R_{\rm shadow}$, and $e_{\rm shadow}$ for all cases considered above. The average radii of the geometrical rings (the dashed lines in

Figures 4, 6, 9, and 13) are included for comparison. In the cases with inclined viewing angles, the procedure given in Section 3.1 for defining the shadow fails. However, we can proceed by reducing the Gaussian-blurring FWHM from 20 to 15 μ as.

In the simple case of viewing a black hole along its spin axis, tilt will break axisymmetry. We consider this viewing angle for Sgr A*. Though the orientation is likely to be different in nature, this model proves instructive. The foreground standing shock that develops in a tilted flow (tilted by 24° in our model) results in local heating, which in turn induces local brightening with the standard electron temperature models. This bright feature approaches small radii in the image. When blurred to a resolution approximating EHT observations, the result is an eccentric shadow.

Table 1 Summary of Model Parameters

	Sgr A* Face-on, Snapshots ^a	Sgr A* Face-on, Averaged	Sgr A* 45°, Averaged	M87, Snapshots ^b
$r_{\rm ring}$				
Geometrical ^c (μas)	24.9	24.9	25.1	19.0
Aligned (µas)	23.50 ± 0.58	23.4	19.8	12.47 ± 0.75
Tilted (μas)	28.0 ± 1.8	28.2	26.2	22.0 ± 3.4
Tilted/aligned	1.191 ± 0.080	1.20	1.32	1.76 ± 0.29
$R_{ m ring}$				
Aligned	0.027 ± 0.010	0.0147	0.0716	0.048 ± 0.012
Tilted	0.052 ± 0.019	0.0304	0.0615	0.083 ± 0.048
Tilted/aligned	2.0 ± 1.0	2.07	0.859	1.7 ± 1.1
$R_{\rm shadow}^{}$				
Aligned	0.021 ± 0.011	0.0203	0.138	0.107 ± 0.028
Tilted	0.136 ± 0.055	0.0998	0.113	0.135 ± 0.047
Tilted/aligned	6.6 ± 4.4	4.92	0.817	1.26 ± 0.55
$e_{ m shadow}^{ m d}$				
Aligned	0.291 ± 0.085	0.209	0.677	0.52 ± 0.13
Tilted	0.69 ± 0.11	0.641	0.653	0.67 ± 0.11
Tilted/aligned	2.36 ± 0.78	3.06	0.964	1.28 ± 0.39

Notes.

Our roughness measure $R_{\rm shadow}$, which quantifies a departure from uniform circularity (a value of 0 is circular), is significantly higher for the tilted case than the aligned case, 0.136 ± 0.055 instead of 0.021 ± 0.011 (dispersion reflecting time variability). Fitting ellipses and measuring eccentricity $e_{\rm shadow}$ shows the same trend, 0.69 ± 0.11 instead of 0.291 ± 0.085 . This is in contrast to the ring itself, whose roughness only increases to 0.052 ± 0.019 from 0.027 ± 0.010 . These same trends hold when analyzing a time-averaged image.

Our ring roughness parameter is defined in a manner similar to the measure of circularity $\sigma_{\rm d}/d$ given in EHT IV (Equations (18) and (19)) and plotted in EHT VI (Figure 18): $2R_{\rm ring} \approx \sigma_{\rm d}/d$. We propose, however, that the power to discriminate between aligned and tilted disks comes more from the shadow properties $R_{\rm shadow}$ or $e_{\rm shadow}$ than from the properties of the ring at peak surface brightness such as $R_{\rm ring}$, based on only the former and not the latter displaying strong statistically significant differences between the aligned and tilted cases we consider.

While the photon ring proper (excluding direct emission) might only become significantly noncircular with modifications to GR (Johannsen & Psaltis 2010), the observed ring of light can obtain noncircular characteristics by merely having the accretion flow be misaligned. Constraining deviations from GR may thus require understanding the tilt of observed systems.

When the same system, whether aligned or tilted, is viewed at a much greater inclination (45°, greater than the tilt angle), the morphology of single snapshots can no longer be captured by a simple shape. Still, time averaging leads to a clear difference between aligned and tilted flows. The radius of the ring is 30% larger in the tilted case, 26.2 μ as compared to 19.8 μ as. The crescent has a symmetric brightness distribution in the aligned case, but in the tilted case the brightest point is not centered (see Figures 8 and 10). In addition, the time-averaged shadow is more eccentric in the tilted case (Figure 8), just as for the face-on viewing angle.

Turning our attention to M87, with a viewing angle of 17° (less than the disk tilt), the effects of tilt become in some ways more dramatic but also somewhat more difficult to describe succinctly. In this case, we turn to even simpler characterizations of the image, which still show differences. Our model of a tilted disk around M87 has a ring size $r_{\rm ring}$ that is $22.0 \pm 3.4~\mu{\rm as}$, compared to $12.47 \pm 0.75~\mu{\rm as}$ in the aligned case.

All else being equal, tilt can increase the size of the observed ring. As this size is used to infer the black hole mass-to-distance ratio M/D, estimates of this ratio may be systematically biased above the true value if tilt exists but is neglected. We note that our tilted model has a ring diameter of $2r_{\rm ring} = 43.9 \pm 6.8~\mu{\rm as}$, compared to the measured value of $41 \pm 1~\mu{\rm as}$ for M87 (EHT VI), meaning our tilted model produces a ring similar in size to that seen in M87 when using a mass of $6.5 \times 10^9~M_{\odot}$.

Our aligned models of M87 are notable in how small the ring appears on the sky given the mass we assume. This is due to a large amount of direct emission appearing inside the photon ring proper. The high-spin, prograde SANE models in the EHT image library also show substantial emission inside the photon ring (EHT V, Figure 2). Note that we fix the parameter $R_{\text{high}} = 10$, and prograde SANE models with R_{high} values this low are ruled out in M87 on the basis of not producing enough jet power. That is, our single aligned model should not be taken to imply that M87, if aligned, must have a mass significantly higher than $6.5 \times 10^9 M_{\odot}$. The EHT library considers more of parameter space, including more a priori viable models, and only in a minority of cases is there such a large amount of foreground emission inside the photon ring proper as in our model. In fact, it is precisely the high-spin, prograde SANE models in the library that lead to the largest inferred M/Dvalues, as shown by the rightmost column of distributions in

^a Uncertainties are standard deviations from 21 snapshots over 11 hr.

^b Uncertainties are standard deviations from 18 snapshots over 2.0 yr.

^c Average radius of the boundary between rays that trace back through the horizon and those that do not.

^d Calculated as described in Section 3.1 for the face-on Sgr A* models, using a 20 μ as blur. For Sgr A* at an inclined viewing angle and for M87, the same procedure is applied but with a 15 μ as blur in order to obtain well-defined shadows.

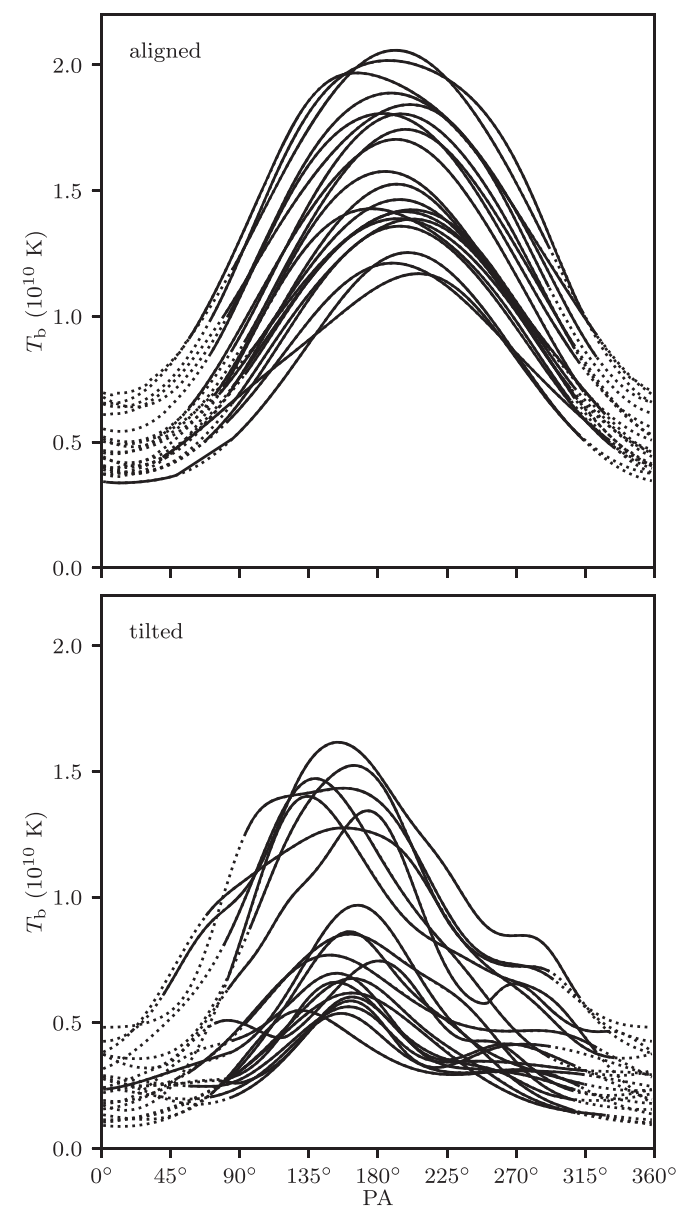


Figure 14. Ridgeline brightness temperatures for 21 snapshots from the aligned (top) and tilted (bottom) simulations, modeled to match M87. The lines are solid where ridgelines are well defined; they are dashed where linear interpolation of radius as a function of position angle is used to locate them (that is, where the solid red lines in Figure 13 are broken). Images of the tilted simulation are clumpier and show more local maxima in these plots.

Figure 8 of EHT V. We have tried varying R_{high} from 1 to 100 and find that ring size does not depend sensitively on this parameter, just as the EHT analysis finds large M/D values in this case for R_{high} from 10 to 80 and even 160 (shown in the same figure).

Another manifestation of the effect of tilt is that of increased clumpiness in the image, as shown in ridgeline brightness profiles like Figure 14. While the first image of M87 from EHT (EHT I) does show multiple bright spots, this can be the result of reconstructing an image from imperfectly sampled, noisy interferometric data, a process that is not particularly well modeled by our simple 20 μ as blurring. For example, Figure 10 of EHT IV shows clumpiness in reconstructions of uniform rings. Thus, the irregularity of the M87 image does not itself

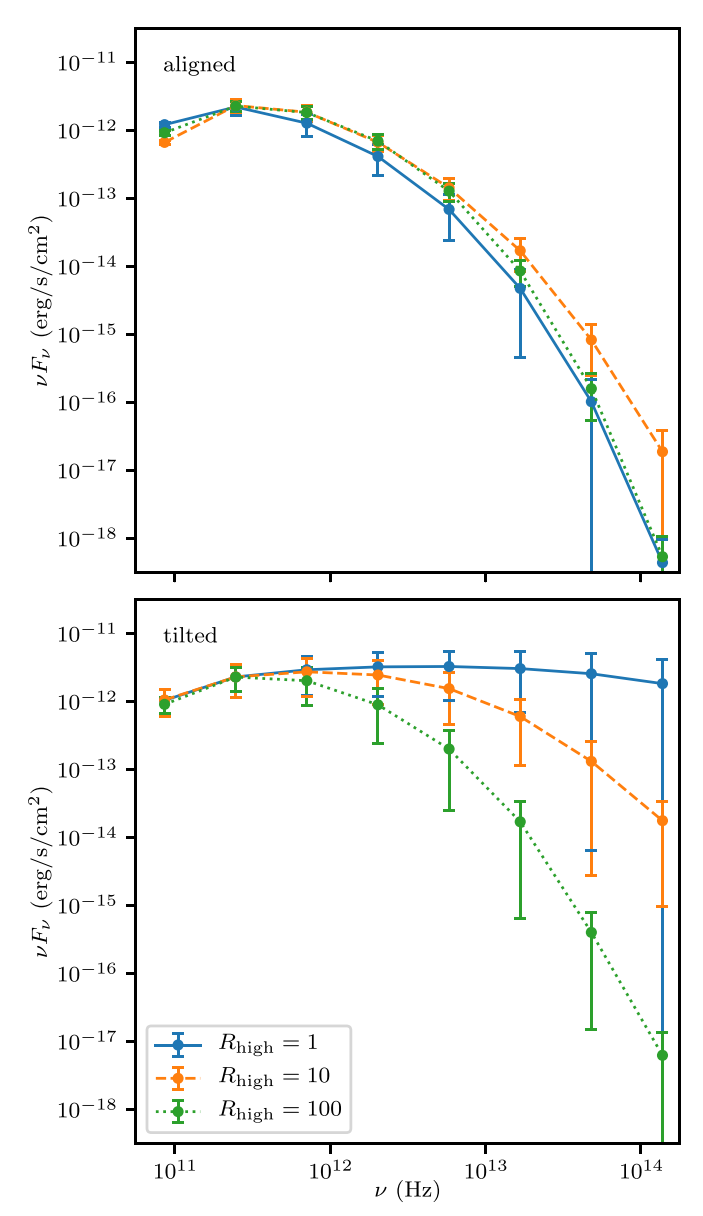


Figure 15. Spectral energy distributions of our models of M87, obtained by ray tracing at eight frequencies from the millimeter to the infrared. Error bars represent standard deviations over the 10 snapshots used, spaced evenly over 1.8 yr. The results for three different R_{high} parameters are shown, each independently normalized to have the same flux at 230 GHz. In the tilted case, the slope of the spectrum is sensitive to R_{high} , which is fixed to 10 throughout the rest of this work.

prove there is a tilted disk, but it would be beneficial for future comparisons of raw data to models to consider tilted cases, complete with their intrinsic bright spots, and to understand what the observational requirements are to detect such clumpiness.

Despite the differences between images of aligned and tilted disks for M87, the latter are not so discrepant with existing data as to be immediately ruled out. For example, with the electron model and blurring adopted here, the morphology we find is still largely ringlike for the tilted case (see Figure 12), in contrast to the two distinct lobes seen in Dexter & Fragile (2013). We also note that the model parameters we adopt produce spectral energy distributions (SEDs) broadly consistent with those observed for M87, as reported in Prieto et al. (2016),

for example. Figure 15 shows the SEDs we obtain in the aligned and tilted cases, using three different $R_{\rm high}$ values. Recent work by Chatterjee et al. (2020) finds that the SED of M87 is well fit by tilted models, and that these models also do well at simultaneously fitting the position angles of the large-scale jet and 230 GHz emission.

We have only examined a single tilted simulation with a single aligned comparison simulation, in order to highlight the most important qualitative differences between the two cases when it comes to horizon-scale observations. Further exploration of this additional parameter is certainly warranted, in order to answer more quantitative questions beyond the scope of this work. For example, the effects we see should grow stronger with increasing tilt, just as the shock heating grows, but the exact dependence is not determined. As tilt approaches 90°, the two-armed spiral pattern may be replaced by a different flow structure. At the same time, there should be spin and tilt angles below which we expect to see essentially the same image as produced by an untilted disk. These upper and lower cutoffs are undetermined.

Here we only consider models in the high-spin, prograde regime. In the EHT library, these differ from low-spin and retrograde models by having a large amount of direct emission inside the photon ring proper. The differences, such as in ring size, that we see between aligned and tilted M87 models may not hold in other portions of parameter space.

Furthermore, the question remains whether these results for largely incoherent magnetic fields apply to the magnetically arrested regime. This is particularly important for application to M87.

Aside from running additional GRMHD simulations to cover more parameter space, there are other lines of inquiry that follow from the same models. We are currently investigating in more detail the effects of tilt on spectral signatures and polarization, in anticipation of further observations and subsequent analyses being completed in the near future.

We thank O. Porth for suggestions for improving the manuscript, as well as A. Spitkovsky for useful discussions about electron heating.

This research was supported in part by the National Science Foundation under grants NSF AST 1715054 and NSF PHY 1748958 and by a Simons Investigator award from the Simons Foundation (EQ). This work used the Extreme Science and Engineering Discovery Environment (XSEDE) Stampede2 at

the Texas Advanced Computing Center through allocation AST170012.

Software: grtrans (Dexter & Agol 2009; Dexter 2016), Athena++ (White et al. 2016).

ORCID iDs

Jason Dexter https://orcid.org/0000-0003-3903-0373 Eliot Quataert https://orcid.org/0000-0001-9185-5044

References

```
Beloborodov, A. M., Levin, Y., Eisenhauer, F., et al. 2006, ApJ, 648, 405
Bird, S., Harris, W., Blakeslee, J., & Flynn, C. 2010, A&A, 524, A71
Blakeslee, J. P., Jordán, A., Mei, S., et al. 2009, ApJ, 694, 556
Blandford, R. D., & Begelman, M. C. 1999, MNRAS, 303, L1
Cantiello, M., Blakeslee, J. P., Ferrarese, L., et al. 2018, ApJ, 856, 126
Chatterjee, K., Younsi, Z., Liska, M., et al. 2020, arXiv:2002.08386
Dexter, J. 2016, MNRAS, 462, 115
Dexter, J., & Agol, E. 2009, ApJ, 696, 1616
Dexter, J., & Fragile, P. C. 2013, MNRAS, 432, 2252
Doeleman, S. S., Fish, V. L., Schenck, D. E., et al. 2012, Sci, 338, 355
Doeleman, S. S., Weintroub, J., Rogers, A. E., et al. 2008, Natur, 455, 78
Fishbone, L. G., & Moncrief, V. 1976, ApJ, 207, 962
Fragile, P. C., & Anninos, P. 2005, ApJ, 623, 347
Fragile, P. C., & Blaes, O. M. 2008, ApJ, 687, 757
Fragile, P. C., Blaes, O. M., Anninos, P., & Salmonson, J. D. 2007, ApJ,
Generozov, A., Blaes, O., Fragile, P. C., & Henisey, K. B. 2014, ApJ, 780, 81
GRAVITY Collaboration 2018, A&A, 618, L10
Johannsen, T., & Psaltis, D. 2010, ApJ, 718, 446
Liska, M., Hesp, C., Tchekhovskoy, A., et al. 2018, MNRAS, 474, L81
Mertens, F., Lobanov, A., Walker, R., & Hardee, P. 2016, A&A, 595, A54
Mościbrodzka, M., Falcke, H., & Shiokawa, H. 2016, A&A, 586, A38
Narayan, R., Mahadevan, R., Grindlay, J. E., Popham, R. G., & Gammie, C.
   1998, ApJ, 492, 554
Paumard, T., Genzel, R., Martins, F., et al. 2006, ApJ, 643, 1011
Prieto, M., Fernández-Ontiveros, J., Markoff, S., Espada, D., & González-Martín, O.
                457, 3801
Shiokawa, H. 2013, PhD thesis, Univ. of Illinois at Urbana-Champaign
The Event Horizon Telescope Collaboration 2019a, ApJL, 875, L1
The Event Horizon Telescope Collaboration 2019b, ApJL, 875, L2
The Event Horizon Telescope Collaboration 2019c, ApJL, 875, L5
The Event Horizon Telescope Collaboration 2019d, ApJL, 875, L6
The Event Horizon Telescope Collaboration 2019e, ApJL, 875, L4
The GRAVITY Collaboration 2019, A&A, 625, L10
Walker, R. C., Hardee, P. E., Davies, F. B., Ly, C., & Junor, W. 2018, ApJ,
   855, 128
White, C. J., Quataert, E., & Blaes, O. 2019, ApJ, 878, 51
White, C. J., Stone, J. M., & Gammie, C. F. 2016, ApJS, 225, 22
Yuan, F., & Narayan, R. 2014, ARA&A, 52, 529
```